

Energy landscape of deformation twinning in bcc and fcc metals

Shigenobu Ogata,^{1,3,4,5} Ju Li,⁶ and Sidney Yip^{1,2,*}

¹Department of Nuclear Science and Engineering, Massachusetts Institute of Technology, Cambridge, Massachusetts 02139, USA

²Department of Materials Science and Engineering, Massachusetts Institute of Technology, Cambridge, Massachusetts 02139, USA

³Handai Frontier Research Center, Osaka University, Osaka 565-0871, Japan

⁴Center for Atomic and Molecular Technologies, Osaka University, Osaka 565-0871, Japan

⁵Department of Mechanical Engineering, Osaka University, Osaka 565-0871, Japan

⁶Department of Materials Science and Engineering, Ohio State University, Columbus, Ohio 43210, USA

(Received 4 November 2004; revised manuscript received 10 February 2005; published 9 June 2005)

Energy landscapes of $(2\bar{1}\bar{1})\langle 111 \rangle$ deformation twinning in bcc Mo and $(111)\langle 11\bar{2} \rangle$ deformation twinning in fcc Al and Cu are determined using density functional theory for sliding of layers numbering up to 7. In bcc Mo, the minimum thickness of a metastable twin is two layers, while twin embryos of three and four layers are unstable. Starting from five layers, the Mo twin can grow in a layer-by-layer fashion. The twin boundary formation and migration energies are found to be 607 and 40 mJ/m, respectively, implying that partial dislocations on twin boundaries will have wide cores and high mobilities. The stress to homogeneously nucleate a partial loop on the boundary of a thick twin is determined to be only 1.4 GPa, indicating that once a deformation twin in Mo reaches a critical thickness, which we estimate to be six layers, it can grow rather easily. Based on simple defect mechanics considerations, we estimate the condition for runaway defect growth requires twin embryo thickness to be tens of layers. Comparing the twinning energy landscape for Mo with those of Al and Cu, we find the former to have a longer ranged interlayer mechanical coupling, which is due to angular bonding and weaker electron screening in the intervening layers. Between Al and Cu, interactions in the former are relatively longer ranged.

DOI: 10.1103/PhysRevB.71.224102

PACS number(s): 62.20.Fe, 61.72.Nn, 61.72.Mm, 61.72.Lk

I. INTRODUCTION

The nature of all plastic dissipation processes in solids is to reduce the free energy by converting elastic strain to inelastic (transformational) strain. Elastic strains tend to be small in amplitude and spatially diffuse, while inelastic strains tend to be large in amplitude and spatially localized. For example, dislocation can be regarded as the bounding rim of a shear shock, one-atomic layer in thickness, inside which the inelastic strain is $|\mathbf{b}|/d_0$, where \mathbf{b} is the Burgers vector and d_0 is the equilibrium interplanar spacing. Outside this shock the inelastic strain is zero,¹ but there exists elastic strain because of diffuse accommodation of the displacement incompatibility at dislocation. Small deviations from the reference (equilibrium) state on the energy landscape are expressed through elastic strains, whereas large deviations manifest through inelastic strains that probe the nonconvexity of the energy landscape. The well-known generalized stacking fault (GSF) energy^{2–8} $\gamma(\mathbf{x})$ represents the energy of inelastically straining the material in the one-atomic-layer thin shear shock as a function of the inelastic shear displacement \mathbf{x} . Because it is a periodic function, $\gamma(\mathbf{b})=\gamma(0)\equiv 0$, ultimately it is energetically favorable to condense any diffuse elastic strain in the bulk into localized one-atomic-layer thin platelet of inelastic strain $|\mathbf{b}|/d_0$ (on the slip plane), because the latter has vanishing energy, whereas the former (elastic strain energy) is always finite and positive.

In the above comparison, we have ignored the energy due to the dislocation, which must accompany any finite-sized shear shock. A dislocation loop of radius R requires a formation energy of $\propto 2\pi R[E_{\text{core}}+K \ln(R/r_0)]$, where E_{core} is the

dislocation core energy,⁹ and K is a combination of elastic constants. So on a per-area basis, the energy cost is only $\propto 2\pi R[E_{\text{core}}+K \ln(R/r_0)]/\pi R^2$ in order to establish unit-area shear shock with inelastic displacement \mathbf{b} . As $R\rightarrow\infty$, the above unit-area cost tends to 0, so it does not affect our argument (that thermodynamically the elastic strain energy cannot compete against arrangements of localized inelastic strains that satisfy the given macroscopic boundary constraint, thus providing the driving force for plastic deformation) in the ultimate sense. But clearly, at finite R , the above energy accounting is of controlling importance in the conversion of elastic strain to localized inelastic strain, which leads to a critical dislocation nucleation size scale R^* and activation energy $\Delta E(R^*)$.¹⁰

Deformation twinning¹¹ is another important mode of strain energy relaxation in metals,¹² and competes with dislocation slip to be the dominant carrier of plasticity. The correlation between energy and defect configuration, as we will find in more detail later, is different since deformation twins can grow in the thickness direction. Indeed, it is often kinetically easier to thicken a twin from n to $n+1$ layers, than to nucleate it from 0 to 2 layers, for example. In this work we will see how and why this is the case for bcc Mo based on first-principles calculations. There is an extra energy per unit area of $2\gamma_{\text{TBF}}$ for deformation twinning which is absent in dislocation full slip, where γ_{TBF} is the twin boundary formation energy. So the energy trade-off is only guaranteed to favor inelastic strain when n , the thickness of the deformation twin, is tending to infinity as well. This is in contrast to full slip where just $R\rightarrow\infty$ is sufficient guarantee. Thus there exists a minimum stress $\tau_n \propto 2\gamma_{\text{TBF}}/n|\mathbf{b}_p|$ for a

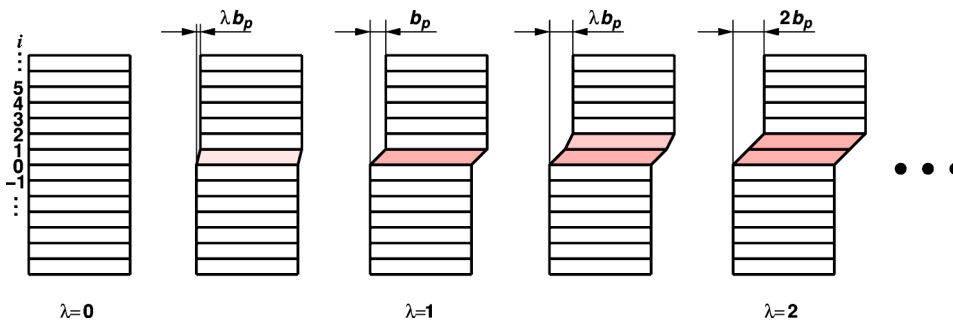


FIG. 1. (Color online) Schematic illustration of the twinning pathway examined. \mathbf{b}_p is partial Burgers vector. See the text for the detail of definitions of the λ and i and sliding plane and direction.

planar twin of fixed thickness n , below which it cannot survive at any size R .

The competition between deformation twinning and full slip depends on the orientation and magnitude of the applied stress,¹³ along with temperature, existing defects such as cracks¹⁴ and intrinsic material properties¹⁵ such as crystal structure and nature of bonding.⁷ It is generally believed that at low to intermediate stress levels, the activation energy for nucleating deformation twin is greater than that of slip. However, once nucleated, a deformation twin is able to produce large amount of inelastic strain within a very short time by thickening. Therefore, deformation twinning tends to occur more frequently under high strain-rate loading such as laser shock,¹⁶ at lower temperatures,¹⁷ and near high stress concentrators.^{12,18} It has been proposed that the kinetics of twin growth, at the mesoscale, involves the pole mechanism¹⁹ and variants,^{20,21} and the double-cross-slip mechanism.^{22,23} On the other hand, information concerning the energetics of the process at the microscopic level has been lacking.

Recently, Tadmor and collaborators establish an intrinsic material property called the “twinability,”¹⁴ which is the ratio of γ_{US} , the unstable stacking energy, to γ_{UT} , the unstable twinning energy, both in J/m^2 . Basically, γ_{US} is the barrier preventing a one-layer partial fault from becoming a one-layer full fault (with zero energy), and γ_{UT} is the barrier against a one-layer partial fault becoming a two-layer partial fault. The assertion that γ_{US}/γ_{UT} fully characterizes twinability implicitly assumes that a two-layer partial fault can be considered a mature twin embryo, or the subsequent evolutions (three-layer, four-layer, ..., partial faults) are similar to the one-layer to two-layer transition, with no additional material properties needed to be introduced. This is true for simple fcc metals as we confirm in this work using density functional theory (DFT) calculations. But using DFT we also find that it is not the case for bcc metals.⁸ Along the twinning pathway of bcc Mo, the fault energy does not manifest steady-state oscillation pattern until $n=6$ layers.

The concept of GSF energy established by Frenkel² and Vitek^{3,4} plays a fundamental role in the understanding of crystalline defects. Its most general form is an energy function $E(\{\Delta\mathbf{x}_i\})$, where $i \in -\infty \dots \infty$ labels sequential atomic stacking planes and $\Delta\mathbf{x}_i$ is the relative shear displacement between plane i and $i+1$. By definition, $E(\{\Delta\mathbf{x}_i\})=0$ when all $\Delta\mathbf{x}_i$'s are zero. Clearly, $E(\{\Delta\mathbf{x}_i\})=E(\{\Delta\mathbf{x}_i+n_i\mathbf{b}\})$, that is, this strain energy is periodic with period \mathbf{b} , the full Burgers vector, which is $\mathbf{b}=[111]a_0/2$ and $[01\bar{1}]a_0/2$ in bcc and fcc crystals, respectively.

We begin with the formulation of our calculation of $E(\{\Delta\mathbf{x}_i\})$ as a function of shear displacements in Sec. II and give results on equilibrium properties as well as on responses at large uniform strains. In Sec. III we describe the calculation of energy landscape and pathway variations with shear displacement, results which would allow us to extract the twin boundary formation and migration energies. We will also show how one can examine the stability of various deformation twin embryos. Twin growth in a layer-by-layer fashion is considered in Sec. IV using the Peierls-Nabarro model for a partial dislocation, and in the following section we consider simple estimates of the local stress at the edge of twin band. In Sec. VI we return to a discussion of the valence charge density distributions that can be extracted from the present DFT calculations, and discuss aspects of interaction range and bond directionality in Sec. VII. We conclude with a concise summary of our results in Sec. VIII.

II. FORMULATION

Recently, two aspects of $E(\{\Delta\mathbf{x}_i\})$ in fcc metals have been probed using electronic-structure calculations.^{6,15} One is to compare side by side a family of functions $\gamma_i(\mathbf{x}) \equiv E(\{\Delta\mathbf{x}_i\})/NS_0$, with $\Delta\mathbf{x}_1=\Delta\mathbf{x}_2=\dots=\Delta\mathbf{x}_N=\mathbf{x}$, all other $\Delta\mathbf{x}_i$'s zero, and S_0 is the cross-sectional area, and study the asymptotic approach of $\gamma_N(\mathbf{x})$ to $\gamma_\infty(\mathbf{x})$, the affine strain energy landscape. This turns out to be a good measure of directional bonding.⁶ The other aspect is examine $E(\{\Delta\mathbf{x}_i\})$ on the so-called twinning pathway, $\gamma_i(\lambda) \equiv E(\{\Delta\mathbf{x}_i\})/S_0$, with $\Delta\mathbf{x}_i=[(\lambda-i)H(\lambda-i)-(\lambda-i-1)H(\lambda-i-1)]\mathbf{b}_p$, \mathbf{b}_p is the partial Burgers vector of the twinning system ($\mathbf{b}_p=[111]a_0/6$ in bcc and $[11\bar{2}]a_0/6$ in fcc), and $H(x)$ is the Heaviside step function (see Fig. 1). In fcc metals, the competition between dislocation nucleation and twin nucleation has been shown to be governed by the values of saddle energies on $\gamma_1(\lambda\mathbf{b}_p)$ and $\gamma_i(\lambda)$, respectively.¹⁴ $\gamma_i(\lambda)$ of fcc metals is relatively simple, possessing a metastable minimum at every $\lambda=n$ for $n=1, 2, 3, \dots$, and converging to a steady oscillating pattern for $\lambda \geq n=2$. In this paper, we show that bcc Mo possesses a much more complicated twinning energy pathway, indicating strong directional bonding and long-range mechanical coupling, with $N=1, 3$, and 4 metastable minima missing, and does not converge to a steady oscillating pattern until $\lambda \geq n=6$. This further enriches the scenario of dislocation-twinning competition in bcc metals, which occurs more often than in fcc metals.

We use the Vienna *ab initio* Simulation Package²⁴ (VASP)

TABLE I. Equilibrium lattice constants (a_0), relaxed (G_r), and unrelaxed (G_u) shear moduli, and bulk modulus (B) of bcc Mo and fcc Al and Cu.

	a_0 [Å]	G_r [GPa]	G_u [GPa]	B [GPa]
Mo $(1\bar{1}0)\langle 111 \rangle$ (Present work)	3.15	126.5	134.5	244.0
[Expt. (Ref. 28), Oth. Calc. (Ref. 29)]	(3.14, 3.10)	(138.7, 129.4)	(142.8, 139.0)	(264, 287)
Mo $(2\bar{1}\bar{1})\langle 111 \rangle$ (Present work)		126.8	134.1	
[Expt. (Ref. 28), Oth. Calc. (Ref. 29)]		(138.7, 129.4)	(142.8, 139.0)	
Mo $(2\bar{1}\bar{1})\langle 111 \rangle$ (Present work)		126.8	134.1	
[Expt. (Ref. 28), Oth. Calc. (Ref. 29)]		(138.7, 129.4)	(142.8, 139.0)	
Al $(111)\langle 11\bar{2} \rangle$ (Present work)	4.04	25.4	25.4	72.4
[Expt. (Ref. 28), Oth. Calc. (Refs. 30 and 31)]	(4.03, 4.04)	(27.4, 22.0 ^a)	(27.6, 27.0 ^a)	(79.3, 74.4)
Cu $(111)\langle 11\bar{2} \rangle$ (Present work)	3.64	31.0	40.9	140.0
[Expt. (Ref. 28), Oth. Calc. (Ref. 32)]	(3.62, 3.64)	(33.3, 39.7)	(44.4, 52.0)	(142, 149)

^aLDA.

with Perdew-Wang generalized gradient approximation²⁵ (GGA) exchange-correlation density functional and ultrasoft (US) pseudopotential.²⁶ The supercell is $\mathbf{e}_1 \times \mathbf{e}_2 \times m\mathbf{e}_3$, with $\mathbf{e}_1 = [111]a_0/2$, $\mathbf{e}_2 = [0\bar{1}\bar{1}]a_0$, and $\mathbf{e}_3 = [2\bar{1}\bar{1}]a_0$, and six atoms per $\mathbf{e}_1 \times \mathbf{e}_2 \times \mathbf{e}_3$ for Mo, with $\mathbf{e}_1 = [11\bar{2}]a_0/2$, $\mathbf{e}_2 = [\bar{1}10]a_0/2$, and $\mathbf{e}_3 = [111]a_0$, and six atoms per $\mathbf{e}_1 \times \mathbf{e}_2 \times \mathbf{e}_3$ for Al and Cu. Brillouin zone (BZ) \mathbf{k} -point sampling is performed using the Monkhorst-Pack algorithm. BZ integration follows the Methfessel-Paxton scheme²⁷ with the smearing width chosen so the “ $-TS$ ” term is less than 0.5 meV/atom. We use 233, 162, and 292 eV planewave energy cutoffs throughout the calculations for Mo, Al, and Cu, respectively.

As benchmark, the perfect crystal properties are computed first. In Table I, the equilibrium lattice constant (a_0) and bulk modulus (B) are compared with experimental results. We then perform direct affine shear in $(1\bar{1}0)\langle 111 \rangle$, $(2\bar{1}\bar{1})\langle 111 \rangle$, and $(3\bar{2}\bar{1})\langle 111 \rangle$ systems for Mo and in $(111)\langle 11\bar{2} \rangle$ for Al and Cu, with the five subsidiary stress components all relaxed and unrelaxed, respectively, to determine the relaxed (G_r) and unrelaxed (G_u) shear moduli.⁷ Experimental values of G_r and G_u are tabulated using analytical formulas (note the degeneracy for small shear) and experimentally measured C_{11} , C_{12} , and C_{44} . Good agreements are found.

We then perform large affine shear, both relaxed and unrelaxed, in $(1\bar{1}0)\langle 111 \rangle$, $(2\bar{1}\bar{1})\langle 111 \rangle$, and $(3\bar{2}\bar{1})\langle 111 \rangle$ for Mo and in $(111)\langle 11\bar{2} \rangle$ for Al and Cu. In Table II, the ideal shear strains and stresses obtained, defined by the point of maximum in the stress-strain response,⁶ are shown. The results for Mo are in good agreement with the first-principles results of Krenn *et al.*³³ The three slip systems of Mo are nearly degenerate in their ideal strains and stresses.

III. DENSITY FUNCTIONAL THEORY RESULTS

Having probed the $\gamma_\infty(\mathbf{x})$ of $(2\bar{1}\bar{1})\langle 111 \rangle$ and others, we now study in detail the $\gamma_t(\lambda)$ pathway on $(2\bar{1}\bar{1})\langle 111 \rangle$. First, we determine the asymptotic behavior of $\gamma_t(\lambda)$ when $\lambda \rightarrow \infty$, i.e., when the twin is very thick and the two twin boundaries are well separated. We expect a steady-state oscillating pattern

$$\gamma_t(\lambda) \rightarrow 2\gamma_{\text{TBF}} + \gamma_{\text{TB}\infty}(\lambda), \quad \text{as } \lambda \rightarrow \infty, \quad (1)$$

in which γ_{TBF} is interpreted as the twin boundary formation energy (unrelaxed), and $\gamma_{\text{TB}\infty}(\lambda)$ the steady-state twin boundary migration energy profile, which is a periodic function in λ with period 1 and with $\gamma_{\text{TB}\infty}(\lambda=0)=0$. We then define $\gamma_{\text{TBM}} \equiv \max_\lambda \gamma_{\text{TB}\infty}(\lambda)$ as the twin boundary migration energy.

TABLE II. Relaxed (γ_m^r) and unrelaxed (γ_m^u) ideal shear strains and relaxed (σ_m^r) and unrelaxed (σ_m^u) ideal shear stresses of bcc Mo and fcc Al and Cu.

Material	Relaxed			Unrelaxed		
	γ_m^r	σ_m^r [GPa]	σ_m^r/G_r	γ_m^u	σ_m^u [GPa]	σ_m^u/G_u
Mo $(1\bar{1}0)\langle 111 \rangle$	0.190	15.18	0.120	0.192	16.52	0.123
Mo $(2\bar{1}\bar{1})\langle 111 \rangle$	0.175	14.84	0.117	0.177	15.99	0.119
Mo $(3\bar{2}\bar{1})\langle 111 \rangle$	0.176	14.87	0.117	0.175	15.93	0.119
Al $(111)\langle 11\bar{2} \rangle$	0.200	2.84	0.110	0.210	3.73	0.147
Cu $(111)\langle 11\bar{2} \rangle$	0.137	2.16	0.070	0.157	3.45	0.084

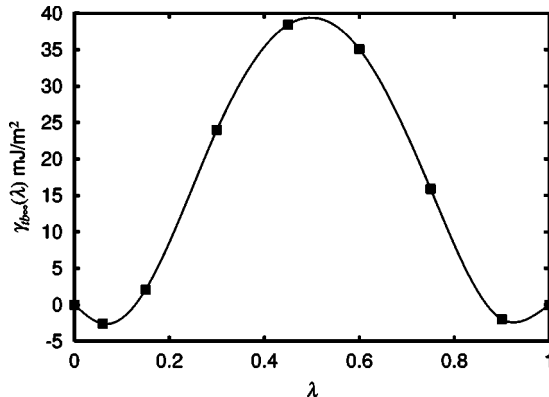


FIG. 2. Energy landscape of twin migration in Mo. Initially a twin boundary is introduced at the center of the 24-layer slab model, and then the boundary position is shifted 1 layer by rigid sliding of the layers on top. The twin boundary migration energy is estimated at 40 mJ/m². The twin boundary formation energy, given by the energy difference between the perfect crystal and twinned bicrystal, is estimated to be 607 mJ/m².

It is the energy barrier per area for a very thick twin to extend one of its boundaries by one layer $\lambda \rightarrow \lambda + 1$. In reality, this is accomplished by an additional twin partial dislocation with Burgers vector \mathbf{b}_p sweeping a face of the twin. According to the Peierls-Nabarro model,^{34–36} the $\gamma_{TB\sim}(\lambda)$ profile controls the width and mobility of the twin partial dislocation. Also, to a large degree, $\gamma_{TB\sim}$ controls the total energy of a “mature” twin and thus the coarse activation energy landscape of twin nucleation. Therefore, it is important to obtain the asymptotic characteristics of $\gamma_i(\lambda)$.

A. bcc molybdenum

To study the behavior of a single twin boundary in bcc Mo, we introduce a slab model with 24 layers of Mo (6e₃ supercell, 2e₃ of which is vacuum), and with 33 × 21 × 1 k-point sampling. No vertical or in-plane relaxation of the atoms in addition to the designated displacements is allowed. The energy of the slab without any twin is evaluated first as a reference. Then, we introduce a configuration whereby layers 1–12 are twinned with respect to layers 13–24. The energy change with respect to the reference is 607 mJ/m², which we designate as γ_{TBF} . It is assumed that a 12-layer or 2e₃ separation from the surface will reduce surface-twin boundary coupling sufficiently. This point will be confirmed independently later in this paper.

We then slide layers 13–24 as a rigid block along \mathbf{b}_p , such that the final configuration has layers 1–13 twinned. The energy profile along this path is plotted in Fig. 2, with the energy at the origin set to be zero. No vertical or in-plane relaxation has been allowed. γ_{TBM} can be estimated from this plot to be 40 mJ/m². If vertical relaxation is allowed, γ_{TBM} can be expected to be further reduced, although not significantly.

An interesting feature of Fig. 2 is that the slope at 0 is not exactly zero. This suggests there is minute in-plane force on layer 13 adjacent to the sharp twin boundary, indicating a slight tendency of the boundary to broaden. This was first

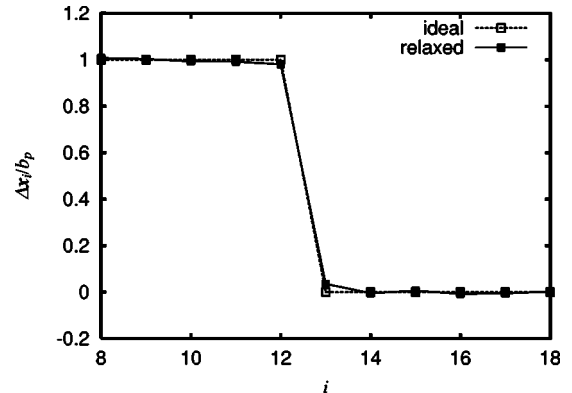


FIG. 3. Difference of layer displacements between adjacent layers $\Delta x_i - \Delta x_{i-1}$ near the ideal and relaxed twin boundary.

suggested by Mrovec *et al.*³⁷ To explore the extent of this effect, we then allow all 24 layers to freely relax in the in-plane directions, until the energy change between two consecutive ionic steps is less than 1 meV. The unrelaxed and relaxed displacements of layers 8–17 are shown in Fig. 3, respectively. We see there is a small relaxation effect, but overall the twin boundary remains very sharp and is a locally stable energy minimum. This partially relaxed twin boundary has an energy of 580 mJ/m².

With the large- λ asymptotic behavior of $\gamma_i(\lambda)$ estimated, we compute $\gamma_i(\lambda)$ at smaller λ using a different setup. Previously, the 24 layers form a twinned-untwinned bicrystal in the supercell. Now, the 24 layers form an untwinned-twinned-untwinned sandwich, with the twinned regions at the center and as far from the surface as possible. Unrelaxed, rigid-block sliding is carried out for each episode of $n \leq \lambda \leq n+1$, that enables the deformation twin to grow by one layer. And then sliding is initiated again in the next layer. The same 33 × 21 × 1 k-point sampling is used, which is found to give converged results. The energy profile is plotted in Fig. 4, with n up to 7, representing a seven-layer twin sandwiched between two untwinned crystals.

We see from Fig. 4 that unlike fcc metals (see Figs. 7 and 8), $\lambda=1$ in bcc Mo is not a metastable state but is unstable. This means there is no metastable one-layer stacking fault in

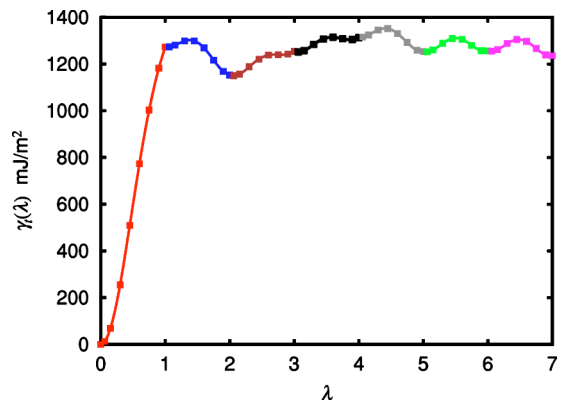


FIG. 4. (Color online) The (2-1-1)(1-1-1) twinning energy pathway of bcc Mo for sliding of layers from 1 to 7 layers in the 24-layer sandwich slab model.

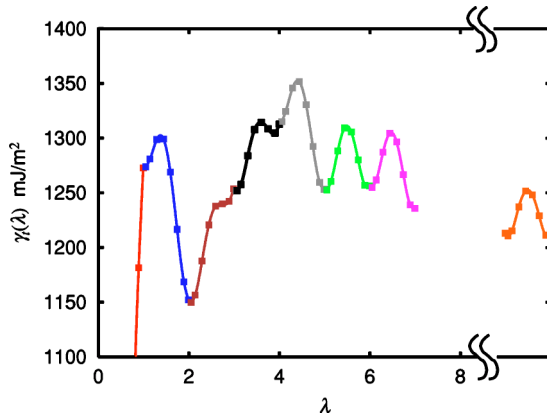


FIG. 5. (Color online) The $(\bar{2}\bar{1}\bar{1})(111)$ twinning energy pathway of bcc Mo up to seven-layer sliding (zoomed). The curve on the right end is Fig. 2 shifted by $2\gamma_{TBF}=1214$ mJ/m².

bcc Mo, so a full dislocation cannot split into partial dislocations with extended one-layer stacking fault between them. However, Fig. 4 shows that the $\lambda=2$ state is metastable. A magnified view is given in Fig. 5. This suggests that the smallest possible twin embryo in bcc Mo consists of two atomic layers. This assertion contradicts with the result obtained using a pair potential,⁴ which states that at least three atomic layers are necessary to form a metastable twin. However, it agrees with calculations^{38,39} using the many-body

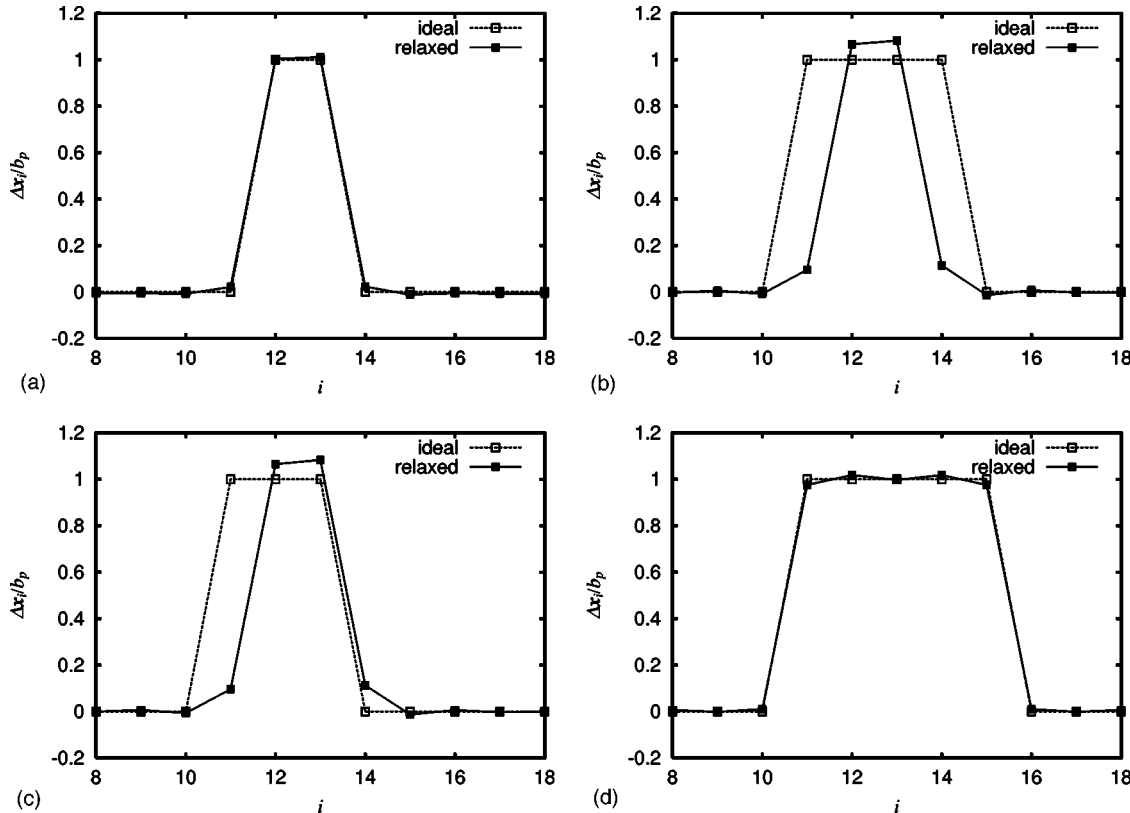


FIG. 6. Difference of shear displacements between adjacent layers $\Delta x_i - \Delta x_{i-1}$ normalized by b_p near the ideal (initial unrelaxed) and relaxed twin embryo configurations. (a) $\lambda=2$, (b) $\lambda=3$, (c) $\lambda=4$, (d) $\lambda=5$. They clearly show that two- and five-layer twin embryos are metastable, while three- and four-layer twin embryos are unstable, which fall back to the two-layer twin embryo configuration spontaneously upon relaxation.

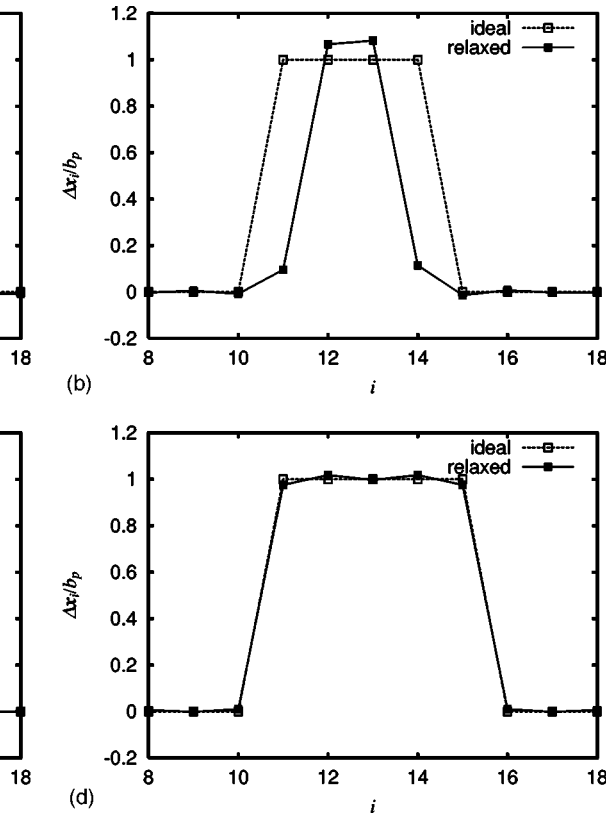
Finnis-Sinclair empirical potential.⁴⁰ To verify that $\lambda=2$ is indeed metastable, we again allow arbitrary in-plane relaxations for all 24 layers in VASP, until the energy change between two consecutive ionic steps is less than 1 meV. The unrelaxed versus relaxed shear displacements of layers 8–17 are shown in Fig. 6(a). We see that aside from slight broadening, the $\lambda=2$ configuration is indeed stable.

Interestingly, the twin that is one layer thicker than the $\lambda=2$ embryo is again unstable. This is seen in Fig. 5. To confirm it, we allow in-plane relaxations with the $\lambda=3$ initial configuration. The initial and final shear displacements are shown in Fig. 6(b). We see that the $\lambda=3$ twin spontaneously relaxes back to the $\lambda=2$ configuration.

The one next, $\lambda=4$, is a borderline case. From Fig. 5, we see there is a small potential energy well at $\lambda=4$. But it is too weak to be trustworthy. Indeed, when we allow in-plane relaxations for all 24 layers in VASP, the $\lambda=4$ twin spontaneously relaxes back to the $\lambda=2$ configuration as shown in Fig. 6(c).

Finally, based on Fig. 5, we believe that starting from $\lambda \geq 5$, every integer- λ state is locally stable. The potential energy wells for $\lambda \geq 5$ appear to be too strong to be destabilized by relaxations, small applied stresses, and numerical error such as surface effects in the calculation. To verify this, the unrelaxed versus relaxed shear displacements of layers 8–17 for $\lambda=5$ are shown in Fig. 6(d).

The practical significance of the above results is the following. Unlike in fcc metals,¹⁴ a twin embryo can only be



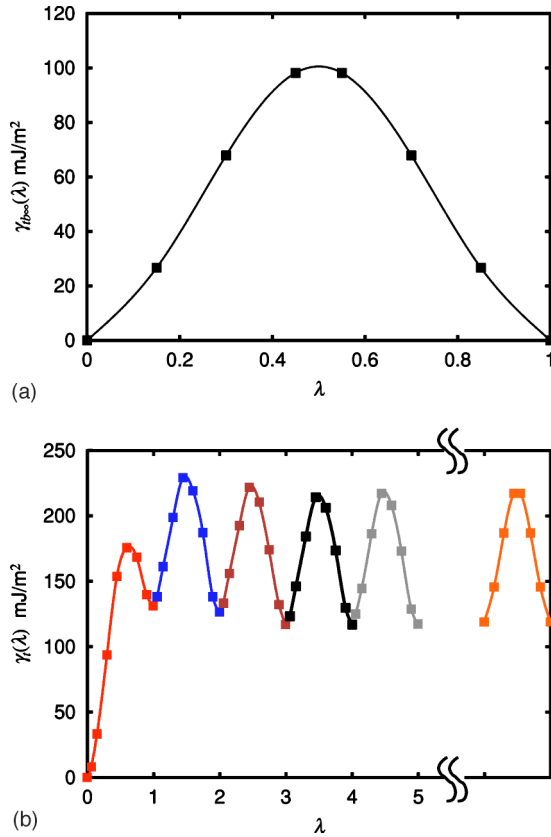


FIG. 7. (Color online) (a) Energy landscape of twin boundary migration in Al using the 24-layer model. The twin boundary migration energy is estimated as 97 mJ/m^2 . (b) The $(111)\langle 11\bar{2} \rangle$ twinning energy pathway of fcc Al up to five-layer sliding using the 24-layer model. The curve on the right end of (b) is just (a) shifted by $2\gamma_{\text{BF}}=120 \text{ mJ/m}^2$.

nucleated in bcc Mo lattice by *simultaneous* emission of two tightly bound partial dislocations. This two-layer twin embryo is however far from mature. The next step is to have an additional group of three tightly bound partial dislocations simultaneously emitted. The Peierls-Rice-Tadmor framework^{14,41} with crack-tip shielding may still be applicable. Now one needs to group the first two partial dislocations as A, and the next three partial dislocations as B, and take into account the “core” shapes of and interactions between A and B, and the detailed $\gamma_t(\lambda)$ response. The mathematics will certainly be different from the fcc case. If one wants to make an analogy with the fcc theory,¹⁴ then the effective “ γ_{UT} ” should be taken to be $\approx 1350 - 1150 = 200 \text{ mJ/m}^2$, which is the energy barrier between the $\lambda=2$ and the $\lambda=5$ energy minima (see Fig. 5).

The potential energy profile of Fig. 5 is a manifestation of long-range mechanical coupling in bcc Mo. A valid question is: if two twin boundaries can couple to each other across five layers, will surface-twin boundary coupling also be long-ranged and thereby contaminate the 24-layer slab calculations, specifically γ_{TB} and γ_{TB} values? While there is no guarantee, we have evidence suggesting that the effect may be small. On the right edge of Fig. 5, we plot $\gamma_{\text{TB}}(\lambda)$ obtained from the bicrystal calculation, shifted by $2\gamma_{\text{BF}}$

$=1214 \text{ mJ/m}^2$. We see that the two calculations (bicrystal and sandwich) seem to give consistent results for the asymptotic behavior. We also perform a few calculations using a 30-layer setup, and the results do not change appreciably from the 24-layer results. Thus, we believe our calculations have converged.

B. fcc aluminum and copper

To study the behavior of an isolated twin boundary in fcc Al and Cu, we introduce the bicrystal slab model with 24 layers of Al ($10\mathbf{e}_3$ supercell, $2\mathbf{e}_3$ of which is vacuum, $18 \times 25 \times 2$ \mathbf{k} -point sampling) and 15 layers of Cu ($6\mathbf{e}_3$ supercell, $1\mathbf{e}_3$ of which is vacuum, $12 \times 17 \times 2$ \mathbf{k} -point sampling). We compute the energy profile $\gamma_{\text{TB}}(\lambda)$ of twin boundary migration for Al [Fig. 7(a)] and Cu [Fig. 8(a)] using the same method as for Mo, and obtain $\gamma_{\text{TB}}=60 \text{ mJ/m}^2$, $\gamma_{\text{TB}}=97 \text{ mJ/m}^2$ for Al, and $\gamma_{\text{TB}}=21 \text{ mJ/m}^2$, $\gamma_{\text{TB}}=168 \text{ mJ/m}^2$ for Cu.

We then set up a sandwich slab model with 24 layers for Al ($10\mathbf{e}_3$ supercell, $2\mathbf{e}_3$ of which is vacuum, $18 \times 25 \times 2$ \mathbf{k} -point sampling) and 15 layers of Cu ($6\mathbf{e}_3$ supercell, $1\mathbf{e}_3$ of which is vacuum, $12 \times 17 \times 2$ \mathbf{k} -point sampling) for Cu, and compute $\gamma_t(\lambda)$ of Al [Fig. 7(b)] and Cu [Fig. 8(b)] in the same way as for Mo. For comparison, $\gamma_{\text{TB}}(\lambda)$ shown in Figs. 7(a) and 8(a) is reproduced at the right end of Figs. 7(b) and 8(b), respectively. We see that the large- λ asymptotic behavior of the sandwich model has converged with the bicrystal model. It is worth noting that in order to keep the relative error due to free surface-twin boundary interaction to less than 5% for up to five-layer sliding, we need to use at least 24- and 15-layer models.

For Cu we see a complete convergence of $\gamma_t(\lambda)$ to $\gamma_{\text{TB}}(\lambda)$ at second layer sliding. However, for Al a slight variation of the energy up to third layer sliding is seen. This indicates that Al has slightly longer ranged layer-to-layer mechanical coupling than Cu, but both are much shorter ranged than Mo. These characteristics will be discussed in Sec. VI.

IV. TWIN PARTIAL DISLOCATION ON THE BOUNDARY OF A THICK TWIN

From Figs. 5, 7, and 8, we see that starting from $\lambda=5$ for Mo and $\lambda=2$ for Al and Cu, the twin should be able to grow in a layer-by-layer fashion. An interesting question is what is the core width of an isolated twin partial dislocation on a very thick twin, when Eq. (1) is applicable. According to the Peierls theory,³⁶ the total energy of the partial dislocation can be expressed as

$$E_{\text{tot}}[\lambda(x)] = - \int \int \frac{K|\mathbf{b}_p|^2}{4\pi} d\lambda(x) d\lambda(x') \ln|x-x'| + \int \gamma_{\text{TB}}[\lambda(x)] dx + \text{const}, \quad (2)$$

under the constraint that $\lambda(-\infty)=0$, $\lambda(\infty)=1$, in which K is an effective modulus (K takes the value of μ for screw dislocation in isotropic medium). Figure 2 shows that $\gamma_{\text{TB}}(\lambda)$ may be well-approximated by

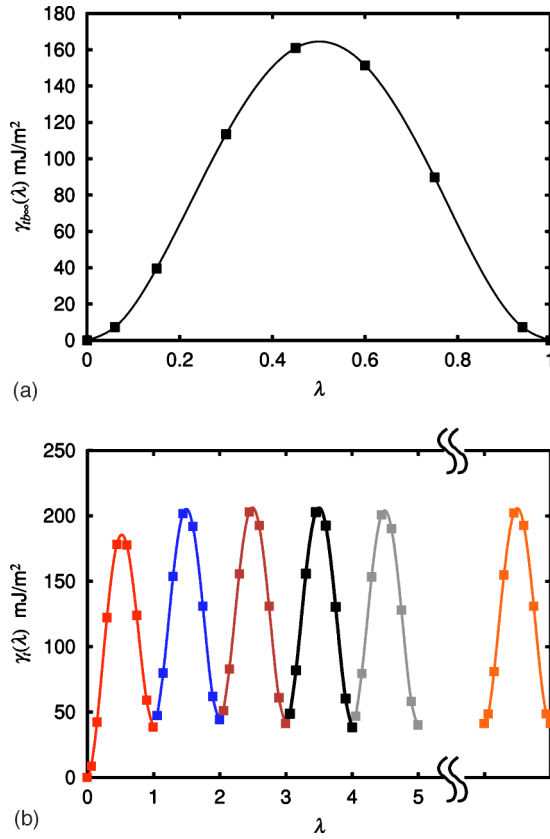


FIG. 8. (Color online) (a) Energy landscape of twin boundary migration in Cu using the 15-layer model. The twin boundary migration energy is estimated as 168 mJ/m². (b) The (111)\langle 11\bar{2} \rangle twinning energy pathway of fcc Cu up to five-layer sliding using the 15-layer model. The curve on the right end of (b) is just (a) shifted by $2\gamma_{TBP}=42$ mJ/m².

$$\gamma_{TB\infty}(\lambda) = \frac{\gamma_{TBM}}{2}(1 - \cos 2\pi\lambda). \quad (3)$$

The above problem has the classic solution

$$\lambda(x) = \frac{1}{2} + \frac{\tan^{-1}(x/\xi)}{\pi}, \quad (4)$$

with

$$\xi = \frac{K|\mathbf{b}_p|^2}{4\pi^2\gamma_{TBM}}. \quad (5)$$

When we plug in $K \approx 140$ GPa and $\gamma_{TBM} \approx 40$ mJ/m² of Mo, we obtain $\xi \approx 7.3$ Å, which is very large since the full width at half maximum (FWHM) of the Burgers vector density (core) distribution

$$\rho(x) \equiv |\mathbf{b}_p|\lambda'(x) = \frac{|\mathbf{b}_p|\xi}{\pi(\xi^2 + x^2)} \quad (6)$$

is 2ξ . This means twin partial dislocations in Mo on thick twins have very wide cores, and very small lattice friction, since the Peierls stress decays exponentially with core width.^{34,35} If we plug in $K \approx 28$ GPa and $\gamma_{TBM} \approx 97$ mJ/m² of Al and $K \approx 44$ GPa and $\gamma_{TBM} \approx 168$ mJ/m² of Cu, we ob-

tain $\xi \approx 2.0$ Å for Al and $\xi \approx 1.5$ Å for Cu, which are almost four times smaller than that for Mo.

To estimate the Peierls stress that is needed to move a twin partial dislocation athermally, we replace the second term of Eq. (2) by a discrete lattice sampling following Nabarro,³⁵

$$\int \gamma_{TB\infty}[\lambda(x)]dx \rightarrow E_{discrete} \equiv \rho_i \sum_{k=-\infty}^{\infty} \gamma_{TB\infty}[\lambda(s + k\rho_i)], \quad (7)$$

where k labels the atomic rows on the (2\bar{1}\bar{1}) plane for bcc Mo and (111) plane for fcc Al and Cu, separated by row spacing ρ_i ($\rho_i = |\mathbf{e}_i|/2$ for fcc and $|\mathbf{e}_i|$ for bcc, $i=1$ for edge and 2 for screw), and s labels the centroid of the rigidly-translating core profile. Plugging in Eq. (4) into Eq. (3), the above sum can be carried out analytically,

$$E_{discrete}(s) = \frac{\pi\gamma_{TBM}\xi \sinh(2\pi\xi/\rho_i)}{\cosh(2\pi\xi/\rho_i) - \cos(2\pi s/\rho_i)} \quad (8)$$

which can be well approximated by

$$E_{discrete}(s) \approx \pi\gamma_{TBM}\xi [1 + 2e^{-2\pi\xi/\rho_i} \cos(2\pi s/\rho_i)] \quad (9)$$

in the limit of large $2\pi\xi/\rho_i$ (here, $2\pi\xi/\rho_1=16.9$, $2\pi\xi/\rho_2=10.3$ for bcc Mo, $2\pi\xi/\rho_1=5.0$, $2\pi\xi/\rho_2=8.7$ for fcc Al, and $2\pi\xi/\rho_1=4.1$, $2\pi\xi/\rho_2=7.1$ for fcc Cu). This energy barrier against centroid translation can be overcome if the applied stress

$$\tau > \tau_p \equiv \frac{\max_s |E'_{discrete}(s)|}{|\mathbf{b}_p|} \approx \frac{4\pi^2\gamma_{TBM}\xi e^{-2\pi\xi/\rho_i}}{\rho_i|\mathbf{b}_p|}. \quad (10)$$

Plugging in the numbers, we find τ_p for Mo is only ~ 2 kPa for the edge partial and ~ 0.9 MPa for the screw partial. Although the above calculation is nonvariational,³⁶ i.e., it assumes rigid core profile translation, we believe that τ_p 's in reality are very small. Thus, unless other resistance mechanisms are operating, a twin partial on a thick twin, once nucleated in bcc Mo, will move very easily and approach the sound speed quickly. We note that the Peierls theory should work better and better in the limit of wide cores, for which this seems to be case.

The small γ_{TBM} also means that it is relatively easy to nucleate a twin partial on the boundary of a thick twin. The stress for athermal (spontaneous) nucleation of a twin boundary dislocation loop on a thick twin is only

$$\tau_{max} = \frac{\max_\lambda |\gamma'_{TB\infty}(\lambda)|}{|\mathbf{b}_p|} = \frac{\pi\gamma_{TBM}}{|\mathbf{b}_p|} \approx 1.4 \text{ GPa} \quad (11)$$

which is rather small, considering the low-temperature macroscopic critical resolved shear stress (CRSS) of bcc Mo is 750 MPa.⁴² In real materials, there are many local stress concentrators such as voids and interstitial clusters. Thus, once a thick enough deformation twin is formed, it should be quite easy to grow in thickness.⁴³⁻⁴⁵

On the other hand, we calculate τ_p for Al as ~ 120 MPa for the twin edge and ~ 5 MPa for the twin screw, and for Cu as ~ 490 MPa for the twin edge and ~ 42 MPa for the twin

screw. Also we estimate τ_{\max} as ~ 1.9 GPa for Al and ~ 3.6 GPa for Cu. If we take into account the respective shear moduli, these numbers are considerably larger than those of Mo in the relative sense.

V. ENERGY LANDSCAPE OF NUCLEATING A RUNAWAY TWIN BAND FROM CRACK TIP

In Sec. III, we compute the elementary energetics involved in the $(2\bar{1}\bar{1})\langle 111 \rangle$ deformation twinning of bcc Mo and the $(111)\langle 11\bar{2} \rangle$ deformation twinning of fcc Al and Cu. In Sec. IV, we apply these results to estimate the core width, mobility and athermal nucleation stress of twin partial dislocation on the boundary of a thick enough twin ($\lambda \geq 6$ for Mo, $\lambda \geq 3$ for Al, and $\lambda \geq 2$ for Cu). Here, we propose to examine the conditions for a “thick enough” twin to be nucleated on the basis of simple defect mechanics.

We begin with the recognition that homogeneous nucleation of deformation twin from defect-free perfect crystal requires a very large activation energy, unless the local stress level approaches the ideal strength of the material,⁷ as in some nanoindentation experiments.^{46,47} Thus, heterogeneous nucleation near existing defects such as cracks, voids, and phase or grain boundaries is necessary. While this may occur in dynamical processes in which inertia plays a role, such as in dynamical fracture or shock loading, here we limit our analysis only to inertia-free, thermally activated nucleation.

Twin nucleation is fundamentally different from nucleation of full dislocations, in the sense that a full dislocation, once nucleated and with large enough radius of curvature R , is a runaway defect, since it does not drag a stacking fault behind. In contrast, for a deformation twin to reach its runaway condition, it needs not only to have a large enough radius in-plane to overcome line tension, but also a critical thickness.¹³ To see this we analyze the canonical model of nucleating a deformation twin band from an atomically sharp crack tip.¹⁰ Consider first the more familiar case of fcc Al. We take the $\gamma_t(\lambda)$ pathway in steady-state oscillating pattern starting from the second layer, and use $2\gamma_{\text{TBF}} = 120$ mJ/m². While a nucleated full edge dislocation (two partials in one plane) in the fcc lattice is a runaway defect, the two-layer twin, because of the finite twin boundary energies $2\gamma_{\text{TBF}}$, will be arrested when the local stress at the leading edge of the twin band drops below

$$\tau_n = \frac{2\gamma_{\text{TBF}}}{n|\mathbf{b}_p|}. \quad (12)$$

For $n=2$, we get $\tau_2=360$ MPa. This suggests that the two-layer twin band cannot get very far from the crack tip after nucleation. Assuming the crack tip stress field falls off as $r^{-1/2}$, as in the case of sharp cracks commonly used in these studies,^{10,14} we estimate the length of the arrested two-layer twin band to be

$$l_n \sim \left(\frac{\tau_{\text{ideal}}}{\tau_n} \right)^2 a_0, \quad (13)$$

in which τ_{ideal} is the ideal shear strength of the material and a_0 is the lattice constant. The rationale behind this crude

estimate is that one needs to apply a K field that generates large local enough stress, approaching the level of ideal shear strength, on the first bond in front of a sharp crack¹⁰ in order to have thermally activated nucleation at reasonable kinetic rates. Plugging in $\tau_{\text{ideal}} \approx 3$ GPa,⁶ we get $l_2 \approx 27$ nm, the distance that a two-layer twin band can move away from the crack tip before it is immobilized by $2\gamma_{\text{TBF}}$.

Next, assume an additional partial dislocation is nucleated on top of the two-layer twin. With $n=3$, we get $\tau_3 = 240$ MPa and $l_3 = 61$ nm. So the three-layer twin band will extend to 61 nm from the crack tip, but is then again immobilized. Similarly, for $n=5$, $\tau_5 = 150$ MPa and $l_5 = 170$ nm; for $n=10$, $\tau_{10} = 73$ MPa, and $l_{10} = 680$ nm, and so on. The thicker the twin, the further it can move away from the crack tip. Eventually, the deformation twin becomes a runaway defect when τ_n drops below the level of the uniform *background* stress applied. Then, the twin no longer needs the crack-tip stress field to balance out the $2\gamma_{\text{TBF}}$ attraction and can propagate on its own. If we take the background stress to be on the same order as the yield stress Y for aluminum, around 100 MPa, then the maximum CRSS = $Y/2 = 50$ MPa. This converts to a runaway condition of $n=15$, for which $\tau_{15} = 49$ MPa. At that point, the 15-layer twin is $l_{15} = 1.5\text{-}\mu\text{m}$ long.

The purpose of the above crude calculation is to demonstrate that there is a coarse energy landscape for the nucleation of a “thick enough” twin in front of a crack that is able to run away, in addition to the finer energetic features involved in the nucleation of each partial. It appears that one needs to add up all the activation energies from $n=1$ to 15 in order to obtain the nucleation barrier of a runaway twin defect, if we assume that the twin embryo is thermalized after each partial dislocation nucleation. In contrast, the nucleation barrier of a runaway full dislocation is much simpler, involving separate nucleations of just two partials within the same plane.

In the above estimate, we ignore the fact that the twin partials would interact with each other to form a lens shape rather than a uniform band, which is what is assumed in Eq. (12). A full calculation seems quite difficult unless numerical schemes such as the phase-field method¹ can be implemented. On a separate note, we think that it is possible that the sum of activation energies from $n=1$ to 20 is a fast decaying sum, such that the strength of the $n=2$ term indicates the comparative magnitude of the sum.

With the fcc case in mind, we now analyze what will happen for bcc Mo. It is more complicated than fcc due to the intricate $\gamma_t(\lambda)$ pathway shown in Fig. 5, which does not manifest steady oscillation until $n=6$. Also, $n=1, 3, 4$ are not metastable minima. So $n=1, 2$ are grouped into A, and $n=3, 4, 5$ are grouped into B in the sum, representing the first two steps of nucleation, followed by layer-by-layer growth. Using the same formulas (12) and (13), but with $2\gamma_{\text{TBF}} = 1214$ mJ/m² and $\tau_{\text{ideal}} \approx 15$ GPa (see Table II), we obtain $\tau_2 = 6.7$ GPa, and $l_2 \approx 1.6$ nm for $n=2$. So the first step of nucleation would give an exceedingly small embryo A extruding from the crack, if that is actually thermodynamically favorable. It would then have to wait for the next step, upon which three new partials are simultaneously nucleated on top of A. This would allow the twin to grow to $\tau_5 = 2.7$ GPa and

$l_5 \approx 10$ nm. Still, $n=5$ is far from the runaway condition. If we plug in CRSS=750 MPa (Ref. 42) as the background stress, we get the runaway condition to be $n=18$, with $\tau_n = 740$ MPa and $l_n \approx 130$ nm.

Note that in the above we assume l_n at runaway is less than the grain size. For nanocrystals¹² this assumption may not be true, and then the behavior again could be quite different. For instance, in Al, if the grain size is around 20 nm, then it is possible for the leading edge of the two-layer twin band to be arrested at the opposite grain boundary. Continuous layer-by-layer twinning of this particular grain in front of the crack can then proceed without having to reach the runaway length first. In the case of bcc Mo, it is not possible to arrest the two-layer twin embryo at the grain boundary because it is too small. However, it is possible that in the next step, the five-layer embryo may be arrested by the opposite grain boundary. And then layer-by-layer deformation twinning of bcc Mo can proceed in this particular nanograin.

VI. ELECTRONIC-STRUCTURE FEATURES

As explained in the Introduction and discussed above, the GSF (Refs. 2–5) and MGSF (Refs. 6–8) corresponding to localized planar shearing modes illustrated in Fig. 1 are the most important elementary energetics controlling the plasticity of metals. It is therefore worthwhile to perform electronic-structure analysis that pertains specifically to these planar shearing modes. One may draw analogy with the Friedel oscillations near a free surface if we consider a surface to be a special kind of planar interface, to which the twin boundary also belongs. Here, the issue is the range of interaction between two twin boundaries. One may consider the difference $\gamma_i(\lambda) - \gamma_{TB\infty}(\lambda)$ as quantifying this effect, which is the influence of one twin boundary's presence on the migratory behavior of another. From Figs. 5, 7(b), and 8(b), it is clear that this twin-boundary–twin-boundary coupling is slightly longer ranged in Al than in Cu, but by far the longest ranged in bcc Mo. The question is: why is this and what electronic-structure features can corroborate this mechanical-response feature?

We hypothesize that the strength of mechanical coupling between two twin boundaries is related to (a) the magnitude of charge perturbation near one twin boundary in reference to the perfect crystal (either one of the two crystal variants, depending on which side of the twin boundary we are doing the comparison) and (b) the potency of dielectric screening of the intervening layers between the two twin boundaries. We may further hypothesize that the (111) planes of fcc metals provide better screening than the (211) planes of bcc metals, since the former are close packed.

We quantify the above considerations by the following measure:

$$\Delta\rho(z) \equiv \frac{\int dx dy |\Delta\rho(x, y, z)|}{\int dx dy}, \quad (14)$$

where

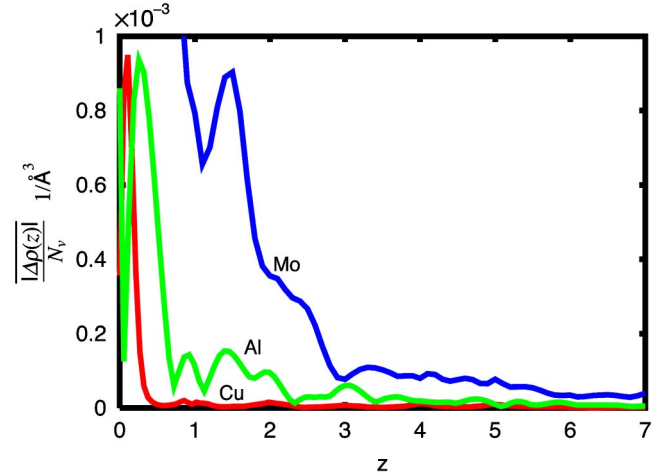


FIG. 9. (Color online) Distribution of valence charge density deviation (with and without twin boundary) for Mo, Al, and Cu. z is distance from twin boundary, normalized by the interlayer distance in \mathbf{e}_3 direction. The charge density is averaged over the plane normal to \mathbf{e}_3 , then normalized by number of valence electrons N_v used in the pseudopotential for each type of atom.

$$\Delta\rho(x, y, z) \equiv \rho(x, y, z) - \rho_{\text{xtal}}(x, y, z). \quad (15)$$

$\rho(x, y, z)$ is the valence charge density of the bicrystal slab. $z=0$ marks the location of the twin boundary, central in the slab. $\rho_{\text{xtal}}(x, y, z)$ is the valence charge density of a slab of perfect crystal, with the same thickness as the bicrystal slab. Depending on $z > 0$ or < 0 , we use $\rho_{\text{xtal}}(x, y, z)$ of the appropriate crystal variant, which are mirror symmetric to each other. Therefore, $\Delta\rho(z)$ is a symmetric function.

$\Delta\rho(z)$ for Mo and Al, Cu are plotted in Fig. 9. The static dielectric response of metals (such as estimated using the Lindhard function) due to sharp spatial features (such as surface/interface) always decays algebraically in real space, so the absolute magnitude of $\Delta\rho(z)$ is important. To make the comparison fair, we normalize $\Delta\rho(z)$ by the number of valence electrons per atom (6 for Mo, 3 for Al, 11 for Cu). It is seen that Mo has by far the largest charge deviations associated with the twin boundary at $z \approx 0$, which persists up to $z \approx 3$. Al is second, with significant charge alteration up to $z \approx 2$. Cu, on the other hand, has very little charge alteration near the twin boundary beyond $z \approx 0.5$.

These data can be used to rationalize the mechanical-response features of Figs. 5, 7(b), and 8(b) in the following way. We may consider doing perturbation theory on the total energy of the perfect crystal sandwiched between two twin boundaries, where $\Delta\rho$'s induced by either boundaries are considered as perturbations. Then, the coupling energy between the two twin boundaries can be written as

$$\Delta E = \int dxdydz \frac{k(x, y, z)}{2} \Delta\rho_1(x, y, z) \Delta\rho_2(x, y, z) + O(\Delta\rho^3), \quad (16)$$

in a second-order expansion around the electronic equilibrium, where $\Delta\rho_1$ is charge alteration caused by the first twin boundary, $\Delta\rho_2$ is charge alteration caused by the second twin

boundary, and $k(x,y,z)$ is the functional expansion coefficient (the first-order term vanishes because we are perturbing around the electronic equilibrium). For simplicity we have assumed the total energy is a local functional of the total charge density

$$k(x,y,z) \equiv \frac{\delta^2 E[\rho(x,y,z)]}{\delta \rho(x,y,z)^2}, \quad (17)$$

and perturbations to the charge density caused by ionic defects are additive. When the two twin boundaries are separated by λ , in a very crude way Eq. (16) may be approximately bounded by

$$\Delta E(\lambda) \propto \int dz \Delta \rho(z) \Delta \rho(\lambda - z). \quad (18)$$

This then can explain why twin-boundary–twin-boundary coupling is so strong in Mo from Fig. 9 comparison, since the coupling strength is really $\Delta \rho$ “squared.” It further explains the interaction range: the coupling energy function $\Delta E(\lambda)$ is a convolution of two $\Delta \rho(z)$ ’s, and do not decay to zero unless λ is outside *twice* the range of z where $\Delta \rho(z)$ decays to zero. Therefore from Fig. 9, we may say that the coupling strength dies off precipitously after $2 \times 3 = 6$ layers in Mo, $2 \times 2 = 4$ layers in Al, and $2 \times 0.5 = 1$ layer in Cu, which is seen from the direct calculations shown in Figs. 5, 7(b), and 8(b).

VII. DISCUSSION

The nature of bonding in condensed matter is often characterized by “interaction range” and “bond directionality.” They are quite distinct concepts. From our previous DFT studies,⁷ we think Al, Cu, and Si have short interaction range (among them Al has relatively longer range), and Mo (maybe also W and Fe) and ionic solids have long interaction ranges. Si has strong directional bonding, and Mo and Al also. Cu and ionic solids have very weak directionality in bonding.

The interaction range, among other things, controls the size of metastable defect embryos such as deformation twins and martensites. So while it is well-known that the smallest fcc twin is two-layers, this is not the case in bcc Mo. This may be partially due to the crystal structure. In fcc metals, the slip planes have larger interplanar spacing and very dense packing in-plane to provide good screening. In contrast, the bcc slip planes are closer in distance, and each slip plane has relatively large “holes,” which causes poor screening.

Yet long-ranged interlayer mechanical coupling may also be partially due to bond directionality. Here we take bond directionality to mean sensitivity to the nearest-neighbor bond angles. For instance near the intrinsic stacking fault of fcc metals, the coordination number of atoms remains the same as in perfect crystal, yet the bond angles are “wrong” compared to fcc bulk. Thus, we may take the much larger intrinsic stacking fault energy of Al compared to Cu as evidence that metallic bonding in Al is bond-angle sensitive, whereas it is not in Cu.^{6,48} Microscopically, bond directionality may manifest as large $\Delta \rho(z)$ near $z=0$, as the charge density reacts strongly to unfavorable bond angles, such as

near a twin boundary. Therefore at the charge-density level, it seems plausible to take $\Delta \rho(z \approx 0)$ as a measure of bond directionality, and the rate of decay of $\Delta \rho(z)$ with z to measure screening. bcc Mo has strong bond directionality and weak screening, which leads to long-ranged interlayer coupling. Cu has weak bond directionality and strong screening, which leads to very short interlayer coupling range. Al has strong bond directionality but relatively strong screening, which leads to short interlayer interaction range. Si has strong bond directionality, but its valence electrons are bound charges, therefore $\Delta \rho(z)$ is short ranged and so is the interlayer coupling.

Clearly, both the range and directionality of bonding in a given material are valuable information for developing empirical interatomic potentials.^{48,49} The simplest kind of interatomic potentials for metals is isotropic and short-ranged similar to the Finnis-Sinclair potential.⁴⁰ However, very short-ranged potentials are clearly incapable of describing long-ranged interlayer mechanical coupling such as Fig. 4. On a similar note, comparing the one-layer GSF $\gamma_1(\mathbf{x})$ with the affine strain energy density $\gamma_\infty(\mathbf{x})$ in DFT provides valuable information about bond directionality,⁶ and many potentials for Al fail in this aspect.⁴⁸ Methodical analysis based on MGSF characterization⁶ and $\Delta \rho(z)$ provide clues on how these potentials may be improved. If the main purpose of an interatomic potential is to study the mechanical behaviors of a material involving dislocations and deformation twins, then this exercise is especially necessary.

VIII. CONCLUSIONS

Because we have touched upon a range of issues in this work, it may be appropriate to conclude with a concise summary of the specific results presented here in a manner that reinforces the statements made in the abstract. We take note first of some baseline results as a way of introducing our first-principles method of calculating energy, stress, and deformation. Table I shows the prediction of lattice parameter and elastic moduli tested against experimental data. The densities of the three metals are seen to be within one percent of the measurements, while the moduli are within 10%. Such accuracy is comparable to similar calculations in the literature. Table II gives the maximum strain that each metal can sustain under affine shear before elastic instability.⁴⁶ While there are yet no measurements of these results which characterize the system far from equilibrium, this information gives insight into the nature of chemical bonding at large strain.⁶ As discussed elsewhere,⁷ knowing this maximum shear strain allows one to formulate a counterpart to the universal binding energy curve, a widely used description of large-strain deformation in tension.

Our studies of deformation twinning are presented in three types of figures. Energy landscape of twin boundary migration $\gamma_{TB\infty}(\lambda)$ gives the energy variation between two specific system configurations (see Fig. 2). The first configuration is a thick stack of twinned region at $\lambda=0$, the initial state. The other is the same system with the twinned region now expanded by exactly one more layer of atoms, the final state at $\lambda=1$. The energy variation from initial to final states

goes through a maximum which defines the twin boundary migration energy. For the three metals the predicted values are 40 mJ/m² [Mo, Fig. 2], 97 mJ/m² [Al, Fig. 7(a)], and 168 mJ/m² [Cu, Fig. 8(a)].

Regarding the issue of stability of twin embryos, we have used the concept of twinning energy pathway $\gamma_t(\lambda)$ (see Fig. 4). This gives the energy variation with sliding (shear) displacement, with integer values of λ corresponding to the shearing of an entire plane. Thus $\lambda=7$ would mean the twinning of a seven-layer stack. One can see from these results that in Mo (Fig. 4) one does not reach convergence until the twinning stack has reached five layers or more, whereas in Al [Fig. 7(b)] and Cu [Fig. 8(b)] convergence is achieved with a stack of only two layers.

These energy landscape results constitute the basis for the statements made in the abstract. In addition, we have examined layer displacement difference $\Delta\mathbf{x}_i/|\mathbf{b}_p|$ (see Figs. 3 and 6) as a measure of stability the twin embryo. A small difference between ideal and relaxed layer displacements would

mean stable embryo, whereas a large difference indicates that the embryo, even if created, is not stable. Thus Fig. 6 shows that the embryo at $\lambda=2$, a two-layer embryo, is stable, but the three- and four-layer embryos are not. Then stability returns for a five-layer embryo. Finally, Fig. 9 portrays the difference between bcc Mo and fcc Al and Cu in their valence charge density distributions. It is information of this type that we feel would be needed to gain a fundamental understanding of materials behavior far from their equilibrium states.

ACKNOWLEDGMENTS

S.O. thanks N. Hirosaki, Y. Shibutani and H. Kitagawa for discussions and acknowledges support by Hattori-Houkoukai fellowship. J.L. acknowledges support by Honda R&D Co., Ltd., NSF, AFOSR, ONR and the Ohio Supercomputer Center. S.Y. acknowledges support by Honda R&D, AFOSR, DARPA, NSF, and LLNL.

*Electronic address: ogata@mech.eng.osaka-u.ac.jp

¹Y. U. Wang, Y. M. Jin, A. M. Cuitino, and A. G. Khachaturyan, *Acta Mater.* **49**, 1847 (2001).

²J. Frenkel, *Z. Phys.* **37**, 572 (1926).

³V. Vitek, *Philos. Mag.* **18**, 773 (1968).

⁴V. Vitek, *Scr. Metall.* **4**, 725 (1970).

⁵J. A. Zimmerman, H. J. Gao, and F. F. Abraham, *Modell. Simul. Mater. Sci. Eng.* **8**, 103 (2000).

⁶S. Ogata, J. Li, and S. Yip, *Science* **298**, 807 (2002).

⁷S. Ogata, J. Li, N. Hirosaki, Y. Shibutani, and S. Yip, *Phys. Rev. B* **70**, 104104 (2004).

⁸S. Ogata, J. Li, and S. Yip, *Europhys. Lett.* **68**, 405 (2004).

⁹J. Li, C.-Z. Wang, J.-P. Chang, W. Cai, V. V. Bulatov, K.-M. Ho, and S. Yip, *Phys. Rev. B* **70**, 104113 (2004).

¹⁰T. Zhu, J. Li, and S. Yip, *Phys. Rev. Lett.* **93**, 025503 (2004).

¹¹J. W. Christian and S. Mahajan, *Prog. Mater. Sci.* **39**, 1 (1995).

¹²M. W. Chen, E. Ma, K. J. Hemker, H. W. Sheng, Y. M. Wang, and X. M. Cheng, *Science* **300**, 1275 (2003).

¹³M. A. Meyers, O. Vohringer, and V. A. Lubarda, *Acta Mater.* **49**, 4025 (2001).

¹⁴E. B. Tadmor and S. Hai, *J. Mech. Phys. Solids* **51**, 765 (2003).

¹⁵N. Bernstein and E. B. Tadmor, *Phys. Rev. B* **69**, 094116 (2004).

¹⁶J. Kaspar, A. Luft, and W. Skrotzki, *Cryst. Res. Technol.* **35**, 437 (2000).

¹⁷S. R. Agnew and T. Leonhardt, *JOM* **55**, 25 (2003).

¹⁸J. Cerv, M. Landa, and A. Machova, *Scr. Mater.* **43**, 423 (2000).

¹⁹A. H. Cottrell and B. A. Bilby, *Philos. Mag.* **42**, 573 (1951).

²⁰A. W. Sleeswyk, *Philos. Mag.* **29**, 407 (1974).

²¹S. Mahajan, *Acta Metall.* **23**, 671 (1975).

²²P. Pirouz, *Scr. Metall.* **21**, 1463 (1987).

²³K. P. D. Lagerlof, *Acta Metall. Mater.* **41**, 2143 (1993).

²⁴G. Kresse and J. Furthmüller, *Phys. Rev. B* **54**, 11169 (1996).

²⁵J. P. Perdew, J. A. Chevary, S. H. Vosko, K. A. Jackson, M. R. Pederson, D. J. Singh, and C. Fiolhais, *Phys. Rev. B* **46**, 6671 (1992).

²⁶D. Vanderbilt, *Phys. Rev. B* **41**, R7892 (1990).

²⁷M. Methfessel and A. T. Paxton, *Phys. Rev. B* **40**, 3616 (1989).

²⁸*Landolt-Börnstein III/14a*, 29a (Springer-Verlag, Berlin, 1992).

²⁹C. Woodward and S. I. Rao, *Phys. Rev. Lett.* **88**, 216402 (2002).

³⁰C. Stampfl and C. G. Van de Walle, *Phys. Rev. B* **59**, 5521 (1999).

³¹D. Roundy, C. R. Krenn, M. L. Cohen, and J. W. Morris, Jr., *Phys. Rev. Lett.* **82**, 2713 (1999).

³²F. Jona and P. M. Marcus, *Phys. Rev. B* **63**, 094113 (2001).

³³C. R. Krenn, D. Roundy, J. W. Morris, and M. L. Cohen, *Mater. Sci. Eng., A* **319**, 111 (2001).

³⁴R. Peierls, *Proc. Phys. Soc. London* **52**, 34 (1940).

³⁵F. R. N. Nabarro, *Proc. Phys. Soc. London* **59**, 256 (1947).

³⁶V. V. Bulatov and E. Kaxiras, *Phys. Rev. Lett.* **78**, 4221 (1997).

³⁷M. Mrovec, T. Ochs, C. Elsässer, V. Vitek, Duc Nguyen-Manh, and D. G. Pettifor, *Z. Metallkd.* **94**, 244 (2003).

³⁸J.-P. Chang, Ph.D. thesis, Massachusetts Institute of Technology, Cambridge, 2002.

³⁹D.-S. Xu, J.-P. Chang, J. Li, R. Yang, D. Li, and S. Yip, *Mater. Sci. Eng., A* **387**, 840 (2004).

⁴⁰M. W. Finnis and J. E. Sinclair, *Philos. Mag. A* **50**, 45 (1984); **53**, 161 (1986).

⁴¹G. Xu, A. S. Argon, and M. Ortiz, *Philos. Mag. A* **72**, 415 (1995).

⁴²H.-J. Kaufmann, A. Luft, and D. Schulze, *Cryst. Res. Technol.* **19**, 357 (1984).

⁴³A. Seeger and L. Hollang, *Mater. Trans., JIM* **41**, 141 (2000).

⁴⁴K. Sumino, *Acta Metall.* **14**, 1607 (1966).

⁴⁵M. Suezawa and K. Sumino, *Phys. Status Solidi A* **36**, 263 (1976).

⁴⁶J. Li, K. J. Van Vliet, T. Zhu, S. Yip, and S. Suresh, *Nature (London)* **418**, 307 (2002).

⁴⁷K. J. Van Vliet, J. Li, T. Zhu, S. Yip, and S. Suresh, *Phys. Rev. B* **67**, 104105 (2003).

⁴⁸R. D. Boyer, J. Li, S. Ogata, and S. Yip, *Modell. Simul. Mater. Sci. Eng.* **12**, 1017 (2004).

⁴⁹J. Li, D. Y. Liao, S. Yip, R. Najafabadi, and L. Ecker, *J. Appl. Phys.* **93**, 9072 (2003).